PHYSICAL REVIEW B **92**, 140506(R) (2015)

Competing magnetic double-Q phases and superconductivity-induced reentrance of C_2 magnetic stripe order in iron pnictides

Maria N. Gastiasoro and Brian M. Andersen
Niels Bohr Institute, University of Copenhagen, Universitetsparken 5, DK-2100 Copenhagen, Denmark
(Received 20 February 2015; published 27 October 2015)

We perform a microscopic theoretical study of the generic properties of competing magnetic phases in iron pnictides. As a function of electron filling and temperature, the magnetic stripe (single-Q) order forms a dome, but competing noncollinear and nonuniform double-Q phases exist at the foot of the dome, in agreement with recent experiments. We compute and compare the electronic properties of the different magnetic phases, investigate the role of competing superconductivity, and show how disorder may stabilize double-Q order. Superconductivity is shown to compete more strongly with double-Q magnetic phases, which can lead to reentrance of the C_2 (single-Q) order, in agreement with recent thermal expansion measurements on K-doped Ba-122 crystals.

DOI: 10.1103/PhysRevB.92.140506 PACS number(s): 74.20.−z, 74.62.En, 74.70.Xa, 74.81.−g

In correlated materials in general, and unconventional superconductors in particular, a microscopic understanding of the magnetism is of paramount importance. Generally, this is because a proper description of the relevant exchange mechanism in these materials is intimately tied to their basic electronic properties. More specifically, it is additionally shown within a wide class of models that the nature of the magnetic fluctuations may be closely linked to the emergence of the superconducting condensate [1–3].

Focusing on the iron-based superconductors, the prevalent magnetic structure consists of collinear magnetic stripe (MS) order with in-plane moments oriented antiferromagnetically (ferromagnetically) along the a (b) axis of the orthorhombic Fe lattice, as shown in Fig. 1(a). Thus, this configuration of moments singles out the $\mathbf{Q}_1 = (\pi,0)$ ordering vector ($1Q$), i.e., $\mathbf{M}(r) = \mathbf{M}_1 \exp(i\mathbf{Q}_1 \cdot \mathbf{r})$. An obvious question, however, is why the system does not take advantage of the enhanced susceptibility at both $\mathbf{Q}_1$ and $\mathbf{Q}_2 = (0,\pi)$ to form other magnetic phases, e.g., double-Q ($2Q$) phases consisting of superpositions of ordering at $\mathbf{Q}_1$ and $\mathbf{Q}_2$ with $\mathbf{M}(r) = \sum_{l=1,2} \mathbf{M}_l \exp(i\mathbf{Q}_l \cdot \mathbf{r})$. This question has been studied theoretically by mainly using various effective field theories restricted to the vicinity of the magnetic transition temperature T_N [4–7]. These works have identified two competing magnetic structures of the $2Q$ type: (1) an orthomagnetic (OM) noncollinear phase with nearest neighbor moments at right angles as shown in Fig. 1(b), and (2) a collinear nonuniform spin and charge ordered (SCO) phase as shown in Fig. 1(c). The favorable magnetic order depends delicately on the band structure, doping level, and interactions [4–7].

Experimentally, the dominating magnetic order in the iron pnictides is the $1Q$ MS state. This phase lowers the C_4 symmetry of the high-T tetragonal phase to orthorhombic C_2, and causes an associated splitting of the crystal Bragg peaks due to magnetoelastic coupling. Recently, several experiments have, however, reported the discovery of magnetic order without an associated structural splitting, i.e., in the tetragonal phase [8,9], which has been taken as indirect evidence for a magnetic driven structural transition in the case of $1Q$ MS order [10]. In the case of $Ba(Fe_{1-x}Mn_x)_2As_2$ [8], however, additional experiments have shown that Mn induce local regions of magnetic (π,π) order and a crystal structure consistent with intertwined short-range clusters of both tetragonal and orthorhombic structure [11–14]. The collective outcomes of these experiments have recently been shown to be captured within a microscopic disorder scenario [15].

The study of $2Q$ order in $Ba(Fe_{1-x}Mn_x)_2As_2$ should be contrasted to other pnictides with out-of-plane dopants where a disorder scenario seems less relevant. This includes, for example, Ba-122 doped with Na or K, where experiments have found evidence for a phase transition into a long-range ordered magnetic phase with tetragonal crystal structure [9,16–21]. For the case of hole-doped $Ba_{1-x}Na_xFe_2As_2$, this magnetic phase exists at the foot of the magnetic dome in the phase diagram [9]. More recently, Böhmer *et al.* used thermal expansion measurements to find a tetragonal low-T phase consistent with a magnetic $2Q$ phase, and additionally revealed a superconductivity-induced reentrant orthorhombic phase at even lower T [17]. Collectively, these experimental findings define the following main challenges for a theoretical description: (1) the existence of $2Q$ phases in restricted (intermediate) doping regimes limited by MS order and superconductivity (SC), (2) the $2Q$ phases exist in a limited (intermediate) T range, (3) SC competes with magnetic order, causing a lowering of T_c upon entering the magnetic $2Q$ phase from the paramagnet, and (4) SC competes more strongly with $2Q$ phases than the C_2 MS, as seen by an upward T_c jump when transitioning from the coexistence phase of SC and $2Q$ magnetism to a coexistence phase of MS order and SC [17].

Here, we perform a study of the stability of, and phase transitions between, the competing magnetic phases obtained from a five-band Hamiltonian relevant to the iron pnictides. The Coulomb interaction is treated within unrestricted self-consistent Hartree-Fock, i.e., all charge and spin densities are allowed to vary at each separate site. These calculations constitute a comprehensive microscopic study of the $2Q$ magnetic phases, also in the presence of SC and disorder, and allows one to access the entire T regime, contrary to previous theoretical studies [4–6,22]. The model provides an explanation of all four challenges outlined above.

The starting Hamiltonian consists of a five-orbital tight-binding band relevant to the pnictides [23] and the usual multiband Hubbard-Hund interaction term. When mean-field

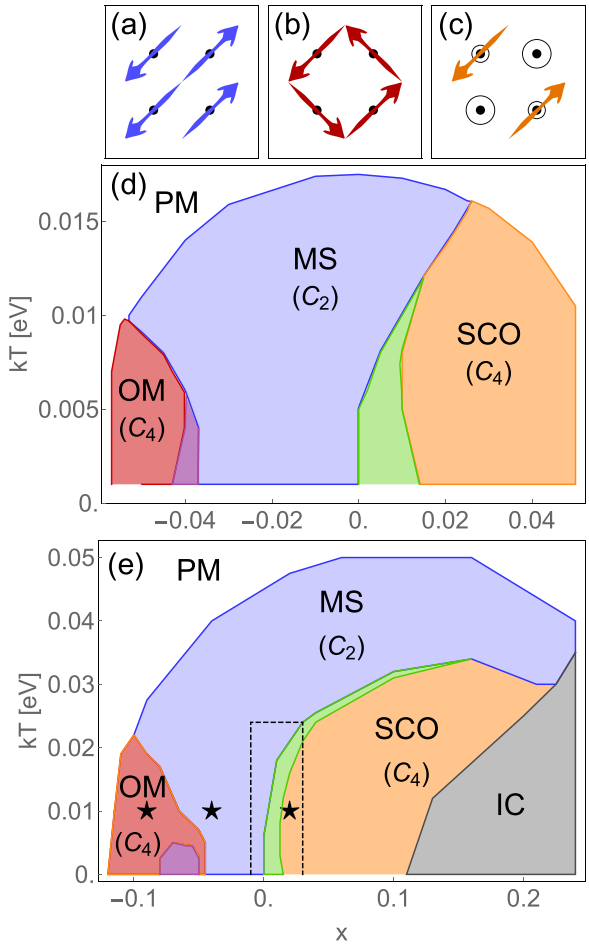

FIG. 1. (Color online) Spin and charge order of the (a) $1Q$ MS ($\mathbf{M_2} = 0$), (b) $2Q$ OM ($\mathbf{M_1} \perp \mathbf{M_2}$), and (c) SCO ($\mathbf{M_1} = \mathbf{M_2}$). The black circles in (c) represent the $\mathbf{Q_1} + \mathbf{Q_2} = (\pi,\pi)$ charge order. (d), (e) Magnetic phase diagrams as obtained from Eq. (1) as a function of T and filling $n_{\rm opt} - x$ for (d) $U = 0.85$ eV and (e) $U = 0.95$ eV. The green (purple) area indicates regions of 2Q phases with $0 < M_1 < M_2$ with collinear $\mathbf{M_1}||\mathbf{M_2}$ (coplanar $\mathbf{M_1} \perp \mathbf{M_2}$) spin structure.

decoupled, this leads to the following model,

$$\mathcal{H}^{\rm MF} = \sum_{ij\mu\nu} (\hat{c}^\dagger_{i\mu\uparrow} \;\; \hat{c}^\dagger_{i\mu\downarrow}) \begin{pmatrix} \varphi^{\mu\nu}_{ij\uparrow} & \omega^{\mu\nu}_{ii\uparrow} \\ \omega^{\mu\nu}_{ii\downarrow} & \varphi^{\mu\nu}_{ij\downarrow} \end{pmatrix} \begin{pmatrix} \hat{c}_{j\nu\uparrow} \\ \hat{c}_{j\nu\downarrow} \end{pmatrix}, \qquad (1)$$

where $c^\dagger_{i\mu\sigma}$ creates an electron at site i with spin σ in orbital state μ. $\varphi^{\mu\nu}_{ij\sigma}$ and $\omega^{\mu\nu}_{ii\sigma}$ are functions of the interaction parameters U, J ($J = U/4$), and the fields $\langle \hat{c}^\dagger_{i\mu\sigma} \hat{c}_{j\nu\sigma'} \rangle$ [see the Supplemental Material (SM) [24]]. We diagonalize Eq. (1) unrestricted on 20×20 lattices, and self-consistently calculate the spin $M^l(\mathbf{r_i}) = \sum_{\mu\sigma\sigma'} \langle \hat{c}^\dagger_{i\mu\sigma} \tau^l_{\sigma\sigma'} \hat{c}_{i\mu\sigma'} \rangle$, and charge density $n(\mathbf{r_i}) = \sum_\mu (\langle \hat{c}^\dagger_{i\mu\uparrow} \hat{c}_{i\mu\uparrow} \rangle + \langle \hat{c}^\dagger_{i\mu\downarrow} \hat{c}_{i\mu\downarrow} \rangle)$, where $l = x,z$, and extract the ordering components $\mathbf{M}_l$ and n_l of $\mathbf{M}(\mathbf{r}) = \sum_l \mathbf{M}_l \exp(i\mathbf{Q}_l \cdot \mathbf{r})$ and $n(\mathbf{r}) = \sum_l n_l \exp(i\mathbf{Q}_l \cdot \mathbf{r})$. We have compared the free energy of the magnetic states $\mathcal{F} = \langle \mathcal{H}^{\rm MF} \rangle - T\mathcal{S}$ to verify the stability of the results, and checked that 100×100 k grids support the same solutions.

Figures 1(d) and 1(e) display two representative phase diagrams as obtained from self-consistently diagonalizing Eq. (1) as a function of T and electron filling for $U = 0.85$ eV [Fig. 1(d)] and $U = 0.95$ eV [Fig. 1(e)]. $n_{\rm opt} = 5.91$ is defined as the electron filling with the highest T_N as deduced by the paramagnetic susceptibility, and the total filling is $n = n_{\rm opt} - x$. The parameter x is directly connected to the electron filling as a deviation from $n_{\rm opt}$ in our model, and not the chemical substitution used in real materials. The fact that the optimal doping level for the magnetic order is offset from $n = 6$ for density functional theory (DFT)-generated bands is well known [25], and not important for the conclusions of this Rapid Communication. As seen from both cases, the $2Q$ phases, OM and SCO, exist at the foot of the MS dome on the electron- and hole-doped sides, respectively, and whereas the transition between the MS and OM phases is sharp, a more gradual transition takes place between the MS and the SCO phases, as indicated by the green intermediate regions. Interestingly, both recent Mössbauer spectroscopy studies of $Sr_{1-x}Na_xFe_2As_2$ [20] and muon spin rotation measurements on $Ba_{1-x}K_xFe_2As_2$ [21] found that indeed the $2Q$ magnetic phase of the hole-doped system seems to be the SCO phase, in agreement with the phase diagrams in Figs. 1(d) and 1(e). The collinear spin structure of the SCO phase was also recently verified by spin polarized neutrons, additionally finding that the moments are oriented along the c axis [26]. The gray area denoted IC in Fig. 1(e) represents an incommensurate magnetic phase where the ordering vectors $\mathbf{Q_1}/\mathbf{Q_2}$ no longer faithfully represent the magnetic ground state of the system. The IC phase is absent in Fig. 1(d) because the lower U leads to a vanishing magnetization at significantly lower doping levels compared to Fig. 1(e).

In the remainder of this Rapid Communication we focus on the $U = 0.95$ eV case, and use the $x = -0.09$ and $x = 0.02$ electron and hole fillings, respectively, to discuss the transition from the MS state to the OM and SCO phases upon lowering T. Figures 2(a) and 2(b) show the T dependence of the spin density wave (SDW) components $M_1 \equiv |\mathbf{M_1}|$ and $M_2 \equiv |\mathbf{M_2}|$ for both fillings. At T_N, M_1 gradually increases while M_2 remains zero, signaling a second-order transition into the MS state. In the $x = -0.09$ case, [Fig. 2(a)], at $T_1 < T_N$, the $1Q$-$2Q$ transition takes place and the moments reorient to form the OM state with $\mathbf{M_1} \perp \mathbf{M_2}$ and $M_2 = M_1$. As seen from Fig. 2(a), the sudden jump of M_2 at T_1 is compensated by a reduction in M_1, leaving the average magnetization $\bar{M}_r = \frac{1}{2}\sqrt{M_1^2 + M_2^2}$ nearly unchanged. In Fig. 2(c) we display the T dependence of the entropy $\mathcal{S}(T)$. The small discontinuity in $\mathcal{S}$ at T_1 [see the inset of Fig. 2(c)] agrees with a weak first-order transition.

The $1Q$-$2Q$ transition taking place at $x = 0.02$ is shown in Figs. 2(b) and 2(d). As seen, in this case the second component M_2 continuously increases below $T_0 < T_N$ in a second-order fashion. The increase of M_2 is again compensated by a decrease in M_1. In this case, however, $\mathbf{M_2}$ is aligned with $\mathbf{M_1}$, and the spin order remains collinear. As soon as $M_2 > 0$, a small charge order is induced at $\mathbf{Q_3} \equiv \mathbf{Q_1} + \mathbf{Q_2} = (\pi,\pi)$ which scales with $\mathbf{M_1} \cdot \mathbf{M_2}$ and thus increases gradually (see SM for more information). In the range $T_1 < T < T_0$, where M_2 is increasing, the system is still C_2 symmetric ($0 < M_2 < M_1$) but has developed characteristics of the SCO state, such as the (π,π) charge order [see Fig. 1(c)]. We stress that this phase, which is a mixture of the MS and SCO phases, is

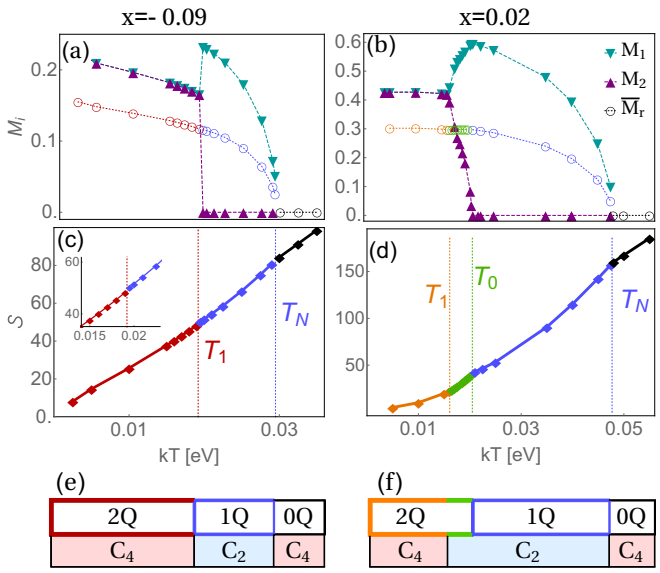

FIG. 2. (Color online) (a) T evolution at $x = -0.09$ of the magnetic components M_1 (▼), M_2 (▲), and $\bar{M}_r = \frac{1}{2}\sqrt{M_1^2 + M_2^2}$ (○), and (c) the entropy $\mathcal{S}(T)$. A zoom of $\mathcal{S}$ at T_1 is shown in the inset. The color changes in $\bar{M}_r$ and $\mathcal{S}$ represent the magnetic phase transitions shown also in Fig. 1(e) with $U = 0.95$ eV. (b), (d) The same as (a), (c) but for $x = 0.02$ with SCO order. (e) and (f) summarize the T dependence of the magnetic structure and the expected associated lattice symmetry.

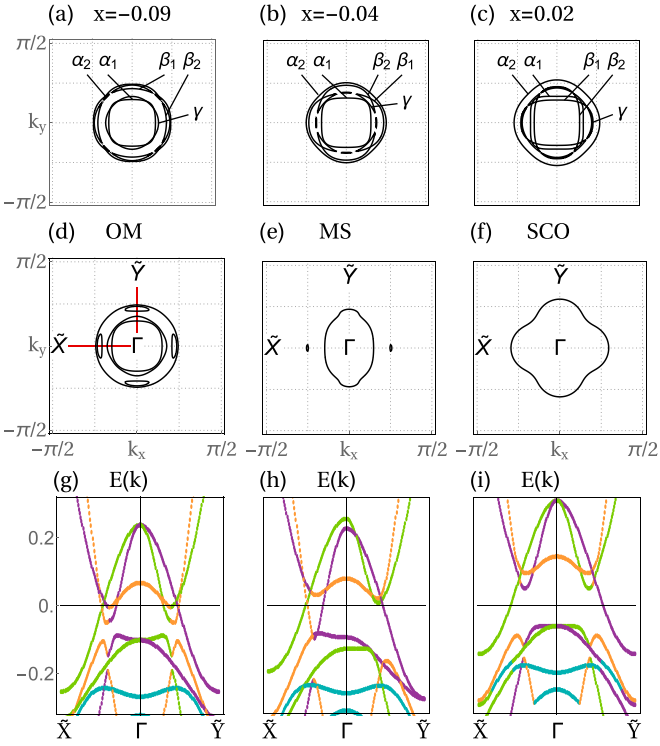

FIG. 3. (Color online) Fermi surface in the folded BZ, $-\pi/2 < k_x, k_y < \pi/2$, in the PM state for (a) $x = -0.09$, (b) $x = -0.04$, and (c) $x = 0.02$, and in the magnetic states (d) OM ($\mathbf{M_1} = 0.2\hat{z}$; $\mathbf{M_2} = 0.2\hat{x}$), (e) MS ($M_1 = 0.52$; $M_2 = 0$), and (f) SCO ($M_1 = M_2 = 0.43$) for $U = 0.95$ eV. (g)–(i) Band structure along the momentum path $\tilde{X}$-Γ-$\tilde{Y}$ shown in (d) for the (g) OM, (h) MS, and (i) SCO phase. The main orbital contributions are shown by purple: d_{xz}; green: d_{yz}; orange: d_{xy}; cyan: d_{z^2}.

not spatially segregated, and is the preferred state found from fully unrestricted real-space lattice calculations. This mixed phase has not been previously discussed, e.g., within Ginzburg-Landau approaches where it is not allowed, unlike the current approach where we have access to all temperatures, including those deep inside the magnetic region. Finally, at $T < T_1$, the pristine C_4 symmetric SCO phase with $M_2 = M_1$ is formed. As can be seen from $\mathcal{S}(T)$ in Fig. 2(d), weak thermodynamic signatures are expected throughout the T range. The T evolution of both transitions and their associated lattice symmetries are summarized in Figs. 2(e) and 2(f).

Next, we compare the electronic properties of the magnetic phases, MS, OM, and SCO, by focusing on the three different fillings indicated by the black stars in Fig. 1(e). In order to illustrate the different nesting conditions, we first show in Figs. 3(a)–3(c) the Fermi surfaces (FS) in the paramagnetic (PM) state in the folded Brillouin zone (BZ) where the X and Y centered elliptical electron pockets β_1 and β_2, and the M centered γ hole pocket all fold on top of the Γ point (see SM for further details). In the ordered state, energy gaps open by the magnetic ordering vector, when their orbital character overlap is nonzero. This is apparent in Figs. 3(a) and 3(d) where the weakly nested β_i and the outer hole pocket α_2 are gapped around $k_x = \pm k_y$ upon the OM formation. The rest of the SDW gaps are opened below the Fermi energy ϵ_F, and the reconstructed bands are seen from Fig. 3(g) to contain considerable orbital mixture. As the filling is increased in Fig. 3(b), multiple electron-hole band crossings get closer to the ϵ_F, and additional nested areas appear at the FS, for example, the ones connected by the γ and β_i pockets. This enhances the spin susceptibility at $\mathbf{Q_1}/\mathbf{Q_2}$, which naturally leads to larger SDW order and more pronounced energy gaps and FS reconstruction in the MS state. The resulting FS in Fig. 3(e) exhibits holelike Dirac cones along the antiferromagnetic (AFM) direction and a hole pocket at Γ of mainly d_{xz} character resulting from the mixing of α_1 and α_2. Evidently, since the MS state singles out the $\mathbf{Q_1}$ ordering vector, the spectrum becomes C_2 symmetric, as shown in Figs. 3(e) and 3(h). Because MS breaks the d_{xz}/d_{yz} degeneracy, an associated ferro-orbital ordering $n_{xz} > n_{yz}$ results in a splitting of the bands at the Γ point, as seen from Fig. 3(h). No such splitting takes place in the $2Q$ states with $M_1 = M_2$ (at least in the absence of spin-orbit coupling). Finally, as the filling is increased further, large nested areas of α_1 and γ with the electron pockets appear at the FS, as seen from Fig. 3(c). For the present band, at this filling the FS nesting is the strongest of the presented cases, and the resulting SDW order parameter and the gaps are the largest. As seen from Fig. 3(f), α_1 and β_i become fully gapped, and similarly most of the γ pocket is gapped except small pieces around $k_x = \pm k_y$ which hybridize with the outermost α_2 pocket. The dependence of the band reconstruction on the interaction parameters is found in the SM.

Motivated by the recent experimental discovery of the effects of superconductivity on the magnetic states [17], we have included SC order to the model by the following BCS term $\mathcal{H}_{\rm BCS} = \sum_{k,\mu\nu} \Delta_{\mu\nu}(k)\hat{c}^\dagger_{k\mu\uparrow}\hat{c}^\dagger_{-k\nu\downarrow}$, where $\Delta_{\mu\nu}(k) =$

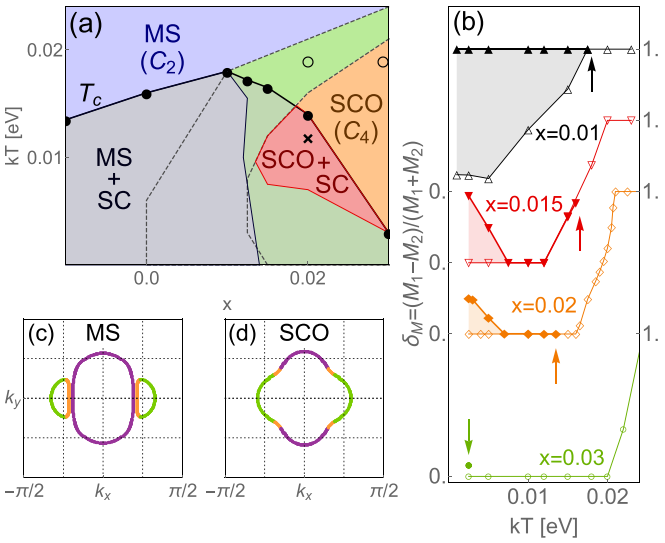

FIG. 4. (Color online) (a) Modified phase diagram from the region indicated by the dashed box in Fig. 1(e) in the presence of SC order. (b) Magnetic anisotropy $\delta_M = (M_1 - M_2)/(M_1 + M_2)$ vs T for four different x with (without) SC order shown by the solid (open) symbols. The arrows mark T_c. (c), (d) Fermi surface at the cross in (a) for MS (c) and SCO (d) order (without SC) using the same orbital color code as in Fig. 3.

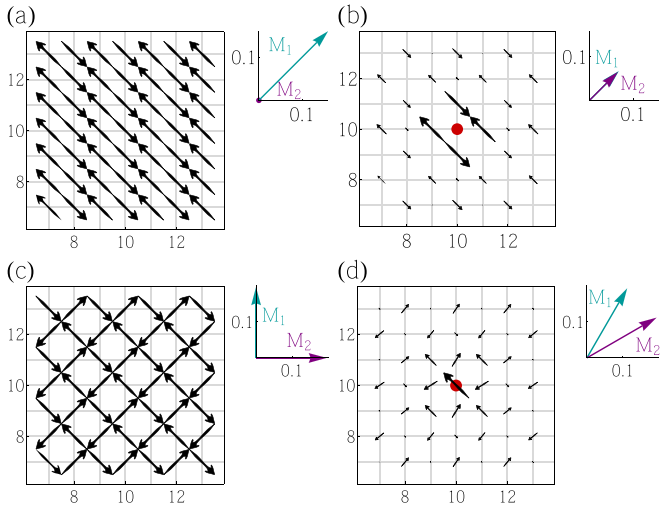

FIG. 5. (Color online) (a), (c) Magnetization at low T and $x = -0.09$ in the absence of an impurity, and (b), (d) in the presence of a single impurity at the center (red dot) with (b) $V = 5$ eV and (d) $V = 2$ eV. The associated Fourier components $\mathbf{M_1}$ and $\mathbf{M_2}$ are also shown [the vectors are normalized to (a) $M = 0.16$, (b) $M = 0.43$, (c) $M = 0.2$, and (d) $M = 0.68$].

$\sum_{k',\alpha\beta} \Gamma^{\beta\nu}_{\mu\alpha}(k-k')\langle \hat{c}_{-k'\beta\downarrow}\hat{c}_{k'\alpha\uparrow}\rangle$. A recent Landau order parameter expansion has also been used to study this problem close to T_N [22]. The effective pairing vertices $\Gamma^{\beta\nu}_{\mu\alpha}(k-k')$ are obtained from the random phase approximation (RPA) spin and charge susceptibilities in the PM state with leading $s_\pm$ symmetry (see SM for details). In order to study the effects of SC on both the $1Q$ and $2Q$ magnetic states, we focus on the region of the phase diagram outlined by the dashed box in Fig. 1(e), and self-consistently solve the associated Bogoliubov–de Gennes equations including both magnetic and SC order parameters. The modified phase diagram shown in Fig. 4(a) exhibits a noticeable effect of SC on the boundaries between both magnetic states, as seen by comparison to the dashed lines indicating the transition lines from Fig. 1(e) without SC order. [The phase diagram corresponding to Fig. 1(d) including superconducting order is supplied in the SM.] Below T_c, where both the magnetic and SC order parameters are nonzero, the MS region expands at the expense of the SCO phase. This effect is explicitly shown in Fig. 4(b) by the evolution of the magnetic anisotropy $\delta_M = (M_1 - M_2)/(M_1 + M_2)$, which is a measure of the C_2 symmetry breaking, i.e., $\delta_M = 0$ ($\delta_M = 1$) for the SCO (MS) state, and $1 > \delta_M > 0$ for mixed C_2 states with $0 < M_2 < M_1$. As seen from Fig. 4(b), without SC, δ_M gradually evolves from $\delta_M = 1$ at high T to $\delta_M = 0$ at low T, with a transition that sharpens with increasing x. In the presence of SC order, however, δ_M is pushed up, as indicated by the shaded regions in Fig. 4(b), and the magnetic order is driven towards the MS phase. This effect is particularly pronounced in the regions of large $\Delta_{\mu\nu}(k)$ closer to the MS phase, and is consistent with recent experiments [17].

The T_c line shown by the solid black dots in Fig. 4(a) evidently exhibits a clear drop across the MS-SCO transition. This reduction of T_c is directly caused by the emergence of the SCO state as verified by the significantly higher T_c (open circles) found by a separate calculation with the magnetic order forced to the MS type. The stronger competition between SC and magnetic order can be explained by a reduced density of states $N(\epsilon)$ at ϵ_F in the SCO phase (compared to MS), $N_{2Q}(\epsilon_F) \sim 0.64 N_{1Q}(\epsilon_F)$. In addition, the dominant SC pairing is the intraorbital d_{xy} element caused by strong γ-β_i FS nesting (see SM). However, as seen explicitly from Fig. 4(d), the FS in the SCO phase (without SC) contains significantly less d_{xy} orbital character (orange points) compared to the corresponding MS FS shown in Fig. 4(c). In summary, T_c is reduced from the PM state into the magnetic phase [$N_{1Q}(\epsilon_F) \sim 0.42 N_{\rm PM}(\epsilon_F)$ and $N_{2Q}(\epsilon_F) \sim 0.26 N_{\rm PM}(\epsilon_F)$], but enhanced from the SCO phase into the MS phase at lower T, in agreement with the experimental finding of Ref. [17].

We end with a brief study of disorder effects on the three magnetic states (without SC) by including the term $\mathcal{H}_{\rm imp} = \sum_{\mu\sigma} V \hat{c}^\dagger_{i^*\mu\sigma}\hat{c}_{i^*\mu\sigma}$ in Eq. (1), relevant for a nonmagnetic impurity at site i^*. Figure 5 summarizes our main findings: Impurities enhance the collinear $2Q$ phase by nucleating local SCO islands. The left column shows the homogeneous magnetic phase without the disorder potential (MS and OM), and the right column the resulting SDW order in the presence of the impurity. As seen, the charge potential acts as a seed for the charge order associated with the SCO phase, and pushes the magnetic order towards the collinear magnetic SCO structure. This can be more clearly seen from the Fourier components $\mathbf{M_1}$ and $\mathbf{M_2}$, also depicted in Fig. 5.

In summary, we have presented a detailed microscopic study of competing magnetic phases in iron pnictides. We have mapped out the phase diagram both in the absence and presence of SC, and found qualitative agreement with recent experimental findings.

We acknowledge useful discussions with A. V. Chubukov, I. Eremin, R. M. Fernandes, and J. Lorenzana, and financial support from a Lundbeckfond fellowship (Grant No. A9318). We thank KITP for their hospitality, where part of this work was initiated and developed.

[1] A. V. Chubukov, Annu. Rev. Condens. Matter Phys. **3**, 57 (2012).
[2] D. J. Scalapino, Rev. Mod. Phys. **84**, 1383 (2012).
[3] A. T. Rømer, A. Kreisel, I. Eremin, M. A. Malakhov, T. A. Maier, P. J. Hirschfeld, and B. M. Andersen, Phys. Rev. B **92**, 104505 (2015).
[4] J. Lorenzana, G. Seibold, C. Ortix, and M. Grilli, Phys. Rev. Lett. **101**, 186402 (2008).
[5] I. Eremin and A. V. Chubukov, Phys. Rev. B **81**, 024511 (2010).
[6] P. M. R. Brydon, J. Schmiedt, and C. Timm, Phys. Rev. B **84**, 214510 (2011).
[7] G. Giovannetti, C. Ortix, M. Marsman, M. Capone, J. van den Brink, and J. Lorenzana, Nat. Commun. **2**, 398 (2011).
[8] M. G. Kim, A. Kreyssig, A. Thaler, D. K. Pratt, W. Tian, J. L. Zarestky, M. A. Green, S. L. Budko, P. C. Canfield, R. J. McQueeney, and A. I. Goldman, Phys. Rev. B **82**, 220503(R) (2010).
[9] S. Avci, O. Chmaissem, S. Rosenkranz, J. M. Allred, I. Eremin, A. V. Chubukov, D. Y. Chung, M. G. Kanatzidis, J.-P. Castellan, J. A. Schlueter, H. Claus, D. D. Khalyavin, P. Manuel, A. Daoud-Aladine, and R. Osborn, Nat. Commun. **5**, 3845 (2014).
[10] X. Wang, J. Kang, and R. M. Fernandes, Phys. Rev. B **91**, 024401 (2015).
[11] G. S. Tucker, D. K. Pratt, M. G. Kim, S. Ran, A. Thaler, G. E. Granroth, K. Marty, W. Tian, J. L. Zarestky, M. D. Lumsden, S. L. Bud'ko, P. C. Canfield, A. Kreyssig, A. I. Goldman, and R. J. McQueeney, Phys. Rev. B **86**, 020503(R) (2012).
[12] Y. Texier, Y. Laplace, P. Mendels, J. T. Park, G. Friemel, D. L. Sun, D. S. Inosov, C. T. Lin, and J. Bobroff, Europhys. Lett. **99**, 17002 (2012).
[13] D. LeBoeuf, Y. Texier, M. Boselli, A. Forget, D. Colson, and J. Bobroff, Phys. Rev. B **89**, 035114 (2014).
[14] D. S. Inosov, G. Friemel, J. T. Park, A. C. Walters, Y. Texier, Y. Laplace, J. Bobroff, V. Hinkov, D. L. Sun, Y. Liu, R. Khasanov, K. Sedlak, Ph. Bourges, Y. Sidis, A. Ivanov, C. T. Lin, T. Keller, and B. Keimer, Phys. Rev. B **87**, 224425 (2013).
[15] M. N. Gastiasoro and B. M. Andersen, Phys. Rev. Lett. **113**, 067002 (2014).
[16] E. Hassinger, G. Gredat, F. Valade, S. R. de Cotret, A. Juneau-Fecteau, J.-Ph. Reid, H. Kim, M. A. Tanatar, R. Prozorov, B. Shen, H.-H. Wen, N. Doiron-Leyraud, and L. Taillefer, Phys. Rev. B **86**, 140502(R) (2012).
[17] A. E. Böhmer, F. Hardy, L. Wang, T. Wolf, P. Schweiss, and C. Meingast, Nat. Commun. **6**, 7911 (2015).
[18] J. M. Allred, S. Avci, D. Y. Chung, H. Claus, D. D. Khalyavin, P. Manuel, K. M. Taddei, M. G. Kanatzidis, S. Rosenkranz, R. Osborn, and O. Chmaissem, arXiv:1505.01433.
[19] B. P. P. Mallett, P. Marsik, M. Yazdi-Rizi, Th. Wolf, A. E. Böhmer, F. Hardy, C. Meingast, D. Munzar, and C. Bernhard, Phys. Rev. Lett. **115**, 027003 (2015).
[20] J. M. Allred, K. M. Taddei, D. E. Bugaris, M. J. Krogstad, S. H. Lapidus, D. Y. Chung, H. Claus, M. G. Kanatzidis, D. E. Brown, J. Kang, R. M. Fernandes, I. Eremin, S. Rosenkranz, O. Chmaissem, and R. Osborn, arXiv:1505.06175.
[21] B. P. P. Mallett, Yu. G. Pashkevic, A. Gusev, Th. Wolf, and C. Bernhard, Europhys. Lett. **111**, 57001 (2015).
[22] J. Kang, X. Wang, A. V. Chubukov, and R. M. Fernandes, Phys. Rev. B **91**, 121104(R) (2015).
[23] H. Ikeda, R. Arita, and J. Kunes, Phys. Rev. B **81**, 054502 (2010).
[24] See Supplemental Material at http://link.aps.org/supplemental/10.1103/PhysRevB.92.140506 for details of the tight-binding band, the mean-field Hamiltonian and additional results.
[25] J. Schmiedt, P. M. R. Brydon, and C. Timm, Phys. Rev. B **85**, 214425 (2012).
[26] F. Waßer, A. Schneidewind, Y. Sidis, S. Wurmehl, S. Aswartham, B. Büchner, and M. Braden, Phys. Rev. B **91**, 060505(R) (2015).